Nanoscale

Ultrafast Relaxation Dynamics in Bimetallic Plasmonic Catalysts

Journal:	*Nanoscale*
Manuscript ID	NR-ART-01-2020-000831.R1
Article Type:	Paper
Date Submitted by the Author:	31-Mar-2020
Complete List of Authors:	Sim, Sangwan; Hanyang University Beierle, Alyssa; New Mexico Institute of Mining and Technology, Chemical Engineering Mantos, Philip; New Mexico Institute of Mining and Technology, Materials Engineering Mccrory, Steven ; New Mexico Institute of Mining and Technology, Materials Engineering Prasankumar, Rohit; Los Alamos National Laboratory, Integrated Nanotechnologies Chowdhury, Sanchari; New Mexico Institute of Mining and Technology, Chemical Engineering

ARTICLE

Ultrafast Relaxation Dynamics in Bimetallic Plasmonic Catalysts

Sangwan Sim[a,b], Alyssa Bierlie[c], Philip Mantos[c], Steven McCrory[c], Rohit P. Prasankumar[a*], and Sanchari Chowdhury[a*]

Received 00th January 20xx, Accepted 00th January 20xx

DOI: 10.1039/x0xx00000x

Combining a plasmonic metal, such as gold, with other popular catalysts, such as Ni or Pt, can extend its benefit to many energy-extensive reactions catalyzed by those metals. The efficiency of a plasmon-enhanced catalytic reaction is mainly determined by the light absorption cross section and the photoexcited charge carrier relaxation dynamics of the nanoparticles. We have investigated the charge carrier relaxation dynamics of gold/nickel (Au/Ni) and gold/platinum (Au/Pt) bimetallic nanoparticles. We found that the addition of Ni or Pt to gold can reduce light absorption in gold nanoparticles. However, electron-phonon coupling rates in Au/Ni and Au/Pt nanoparticles are significantly faster than that of pure Au nanoparticles. This is due to the fact that both Ni and Pt possess significantly larger electron-phonon coupling constants and higher densities of states near the Fermi level in comparison to Au. Additionally, the phonon-phonon coupling rate of bimetallic Au/Pt and Au/Ni nanoparticles was significantly different than that of pure gold nanoparticles, due to the acoustic impedance mismatch at the nanoparticle/substrate interface. Our findings provide important insights towards the rational design of bimetallic plasmonic catalysts.

1. Introduction:

The design of novel catalysts using plasmonic nanostructures, which can efficiently exploit light to accelerate energetically demanding chemical reactions, is of both economic and environmental interest. Plasmonic nanoparticles (NPs) such as gold are particularly attractive for this purpose, as they can harvest incident light in nanoscale volumes to produce excited charge carriers. The photoexcited electrons can decay through two different pathways: (i) radiatively, through the reemission of a photon, or (ii) non-radiatively, creating a transient population of non-equilibrium (hot) charge-carriers. The hot electrons will eventually release their energy to the nanostructure in the form of heat, thus increasing its temperature. The photoexcited charge carriers can also be directly transferred to an adsorbed reactant molecule with favorable energy levels. Both photothermal effects and excited electron transfer from plasmonic nanoparticles can be used to enhance the efficiency of numerous industry-relevant reactions,[1, 2] such as selective hydrogenation of styrene and alkene[3, 4], Suzuki coupling reactions[5], steam reforming[6], alcohol oxidation[7], and polymerization[8, 9]. However, most highly active catalysts used in industry, such as Pt and Ni, are not good at harvesting visible light to generate excited electrons. To circumvent this limitation, recently there has been interest in coupling the highly active catalysts Pt, Pd and Ni with the strong plasmonic metals Ag and Au to generate bimetallic plasmonic catalysts.[3, 9, 10, 11, 12,13,14] Combining Au with Pt and Ni can extend the benefits of plasmonic NPs to any energy-extensive industrial processes accelerated by those catalytically active metals.[10, 11, 15-19] However, the relaxation dynamics of photoexcited electrons in these systems have significant implications on the selection of plasmonic catalyst. While larger electron-phonon and phonon-phonon coupling in nanoparticles, resulting in short relaxation times, are desirable for photothermal heat generation, they adversely affect hot electron transfer.[2] Therefore, a systematic understanding of the energy dissipation rate of photoexcited charge carriers, which is fundamental for the performance of those bimetallic plasmonic catalysts, is still lacking.[20]

One can address this by studying the optical properties and relaxation dynamics of excited electrons in these nanostructures with ultrafast optical spectroscopy. After femtosecond optical photoexcitation, non-equilibrium electrons in plasmonic NPs relax via electron-electron coupling on a very short time scale (tens of femtoseconds), giving rise to a "hot" electron distribution around the Fermi level. The excited electrons further equilibrate with the nanocrystal lattice through electron–phonon coupling on a time scale of a few picoseconds. Subsequently, heat is released to the surrounding medium on a time scale of hundreds of picoseconds to generate a photothermal effect.[1, 2, 20-26] The relaxation dynamics are a strong function of the electron-phonon coupling constant, electronic heat capacity and the band structure of the constituent metals. Additionally, the interfacial thermal conductance plays an important role in heat transfer from a plasmonic catalyst to adsorbed molecules, which depends on the electron-phonon coupling rate.[27] All the above properties are a strong function of material composition. Importantly, these properties are very different for gold than other catalysts, such as platinum and nickel, as can be seen in table 1 of the Supporting Information (SI). Both Pt and Ni possess

[a] *Center for Integrated Nanotechnologies, Los Alamos National Laboratory, Los Alamos, New Mexico 87545*
[b] *Division of Electrical Engineering, Hanyang University, Ansan 15588, Korea*
[c] *Chemical Engineering Department, New Mexico Tech, Socorro, NM-87801*
[d] **rpprasan@lanl.gov , *sanchari.chowdhury@nmt.edu*
Electronic Supplementary Information (ESI) available: [details of any supplementary information available should be included here]. See DOI: 10.1039/x0xx00000x

significantly larger electron-phonon coupling constants and density of electrons near the Fermi energy in comparison to Au. Hence, the addition of a catalyst such as nickel or platinum to plasmonic gold NPs can significantly alter their electron-phonon coupling, in turn influencing the photothermal conversion efficiency. However, our understanding of how adding these catalytic materials to the plasmonic metal can influence the relaxation dynamics is still very limited. Here, we have applied ultrafast optical spectroscopy to examine the rate of different plasmon dephasing pathways, electron-phonon coupling, and phonon-phonon coupling in bimetallic nanoparticles. Our results demonstrate that the addition of Pt or Ni to gold nanoparticles enables us to control their optical properties and carrier relaxation dynamics, which could make it possible to employ them in a much wider range of applications.

2. Experimental Methods:

The nanoparticles were synthesized using an electron beam evaporation method. A 5 nm Au thin film was first deposited on a glass substrate using e-beam evaporation, after which it was annealed at 400 degrees Celsius for two hours in order to synthesize gold nanoparticles. These gold nanoparticles are subsequently coated with a thin layer of Ni or Pt using e-beam evaporation to get bimetallic nanostructures. The morphology and material properties of all of the nanoparticles were characterized using high-resolution transmission electron microscopy (HRTEM), energy-dispersive X-ray spectroscopy (EDX), and UV-Vis spectroscopy. For HRTEM, the nanoparticles were deposited on a TEM grid with nine silicon dioxide 20 nm thick windows, purchased from TEM Windows, a division of SIMPore Inc. The nanoparticles were deposited on the TEM grid following the same procedure mentioned above for the glass substrate. Please note that TEM grids with silicon dioxide windows are chosen to mimic the processing conditions on the glass substrate.

Our ultrafast pump-probe spectroscopy setup is based on a 100 kHz Ti:sapphire regnerative amplifier centered at 800 nm, the output of which is split into two arms. One arm is frequency-doubled in a BBO crystal to generate pump pulses at 400 nm. Another arm is focused into a sapphire disk to generate white-light-continuum probe pulses. Pump and probe beam spot diameters at the sample are ~300 µm and ~150 µm, respectively. The probe beam transmitted through the sample is detected by a photodetector after wavelength selection by a monochromator. The full width at half maximum of the cross-correlation of the pump and wavelength-dependent probe pulses is ~ 100 fs. We measure ΔT/T, where ΔT is the pump-induced change in the intensity of the transmitted probe, and T is the transmitted probe intensity without the pump.

3. Results and Discussion:

In order to avoid the influence of ligands or capping agents on the relaxation dynamics, the gold nanoparticles were synthesized by annealing a 5 nm Au thin film deposited using e-beam evaporation. [28] Using this method, the gold nanoparticles are produced due to thermal dewetting (Figure 1(a)).[29] These gold nanoparticles were subsequently coated with a thin layer of Ni or Pt using e-beam evaporation. Gold nanoparticles can act as nucleation centers for the other metals to produce bimetallic nanoparticles.[30] This method mostly produced bimetallic Au/Ni or Au/Pt nanoparticles, and the nucleation of pure platinum or nickel nanoparticles was very rare (Figures 1(b) and 1(c)). The HRTEM images of Au/Pt (Figure 1(e)) and Au/Ni nanoparticles (Figure 1(f)) show that Pt and Ni atoms diffused into the gold core to produce more alloy-like structures. TEM energy-dispersive X-ray spectroscopy (EDX) data suggested the composition of the bimetallic nanoparticles is ~96% gold, with the rest Pt or Ni (Figures 1(g) and 1(h)). The size of the gold nanoparticles deposited was 30± 7 nm. The sizes of Au/Ni and Au/Pt nanoparticles were 32± 9 nm and 35±9 nm, respectively. The size distribution histograms for the Au, Au/Ni and Au/Pt bimetallic nanoparticles are given in figure S1 in the SI.

Optical spectroscopy revealed that as expected, Au nanoparticles exhibit a distinct absorption band with a maximum around 550 nm (Figure 2(a)). The UV-vis extinction spectra of both Au/Ni and Au/Pt nanoparticles show a slight red shift and broadening of the gold surface plasmon band relative to that of bare Au nanoparticles, which is due to changes in the size and dielectric constant of the nanocomposites with respect to pure gold nanoparticles.[31, 32,33,34]

For all of our samples, photoexcitation was initiated with a 400 nm, ~100 femtosecond (fs) pump pulse, and the relaxation dynamics were probed across the visible regime (λ_{probe} = 450–750 nm) at room temperature using femtosecond white light pulses. We note that from figure 2(a), the bimetallic NPs show higher absorption at 400 nm than the bare Au nanoparticles. Figure 2 shows the temporal evolution of the normalized differential transmission ($\boldsymbol{\Delta T/T}$) spectra for all the nanoparticles. All of the spectra exhibit a positive transient bleach of the surface plasmon resonance around 550 nm, matching their steady state absorbance peak. In all of the nanoparticles, the peak of the transient bleach steadily blue-shifts back towards the plasmon resonance as the electron gas cools. The wavelength at which the differential transmission signal transitions from positive to negative on the red side of the plasmonic peak (550 nm) also blue-shifts with increasing time. This observation is consistent with previous ultrafast studies of hot-carrier dynamics in metal nanoparticles on SiO_2 substrates,[35, 36] and usually happens due to the decrease of both the magnitude and width of the transient spectrum with temperature.[31] The negative wings on both sides of the plasmon band are usually due to pump-induced transient broadening of the plasmon resonance and depend on the shape of the steady-state absorption spectrum. Au nanoparticles have sharp steady-state peaks; hence we see clear negative wings at both lower and higher wavelengths. The steady-state absorption spectra of Au/Ni and Au/Pt nanoparticles have gentle slopes, especially in the long wavelength region, which likely causes the negative wings to lie outside our measured wavelength range.

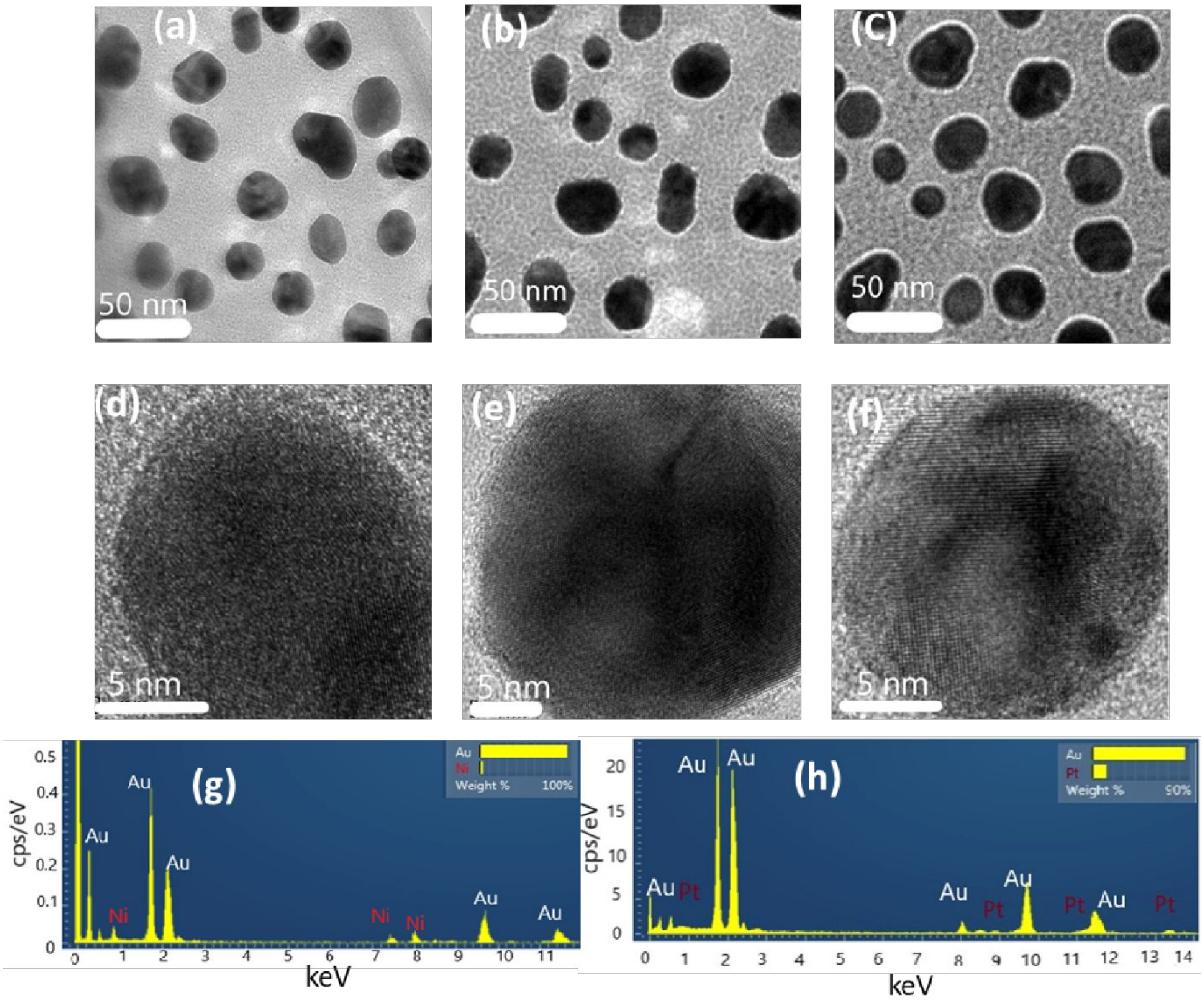

Figure 1: TEM images of (a) Au, (b) Au/Ni, and (c) Au/Pt nanoparticles. HRTEM images of (d) Au, (e) Au/Ni, and (f) Au/Pt nanoparticles. (g) TEM-EDX spectrum of Au/Ni nanoparticles. (h) TEM-EDX spectrum of Au/Pt nanoparticles.

Figure 3(a) shows differential transmission (ΔT/T) traces for different nanoparticle samples at a wavelength corresponding to the plasmon peaks in the sample-dependent transient spectra of Figure 2. Both Au/Ni and Au/Pt nanoparticles exhibit significantly faster decay dynamics than pure Au nanoparticles. The differential transmission traces for all the nanoparticles are fit with a sum of exponentials convolved with a Gaussian function to account for the pump and probe pulse durations.[37] The details of the differential transmission trace fitting are provided in section 3 of the Supporting Information. While the fast decay component ranges from a few hundred fs to a few picoseconds (ps) (Figure 3(b)), the slow decay component is extremely long (a few hundred ps). The fast decay component ($\boldsymbol{\tau_{e-ph}}$) can be attributed to electron-phonon (e-ph) coupling, as in other studies of ultrafast dynamics in metal nanoparticles.[35, 38, 39] The longer decay constant is assigned to the cooling rate of the nanoparticles through energy exchange with their environment via phonon-phonon coupling.[35, 40, 41]

At the pump fluences used in our experiments (5-78 μJ/cm^2), the initial change in the electron temperature is expected to be <220 K (see the SI for the temperature calculation). In this temperature range, the coupling between hot electrons and phonons that leads to the fast decay component in our data is often described using a two-temperature model.[42, 43] According to this model, at low initial electronic temperatures the electron-phonon decay time $\boldsymbol{\tau_{e-ph}}$ can be modeled using the following equation,[44]

$$\boldsymbol{\tau_{e-ph}} \approx \frac{\boldsymbol{\gamma(Temp_0 + \Delta Temp)}}{\boldsymbol{g}}, \qquad (1)$$

where g is the electron–phonon coupling constant, $\boldsymbol{\gamma}$ is the electron heat capacity constant, $Temp_0$ is the ambient temperature, and $\boldsymbol{\Delta Temp}$ is the temperature increase induced by the pump laser.

The temperature increase is proportional to the absorbed energy density; hence according to the above equation $\boldsymbol{\tau_{e-ph}}$ should vary approximately linearly with the absorbed energy density. In order to verify that, we conducted transient absorption experiments as a function of pump laser fluence. The values of $\boldsymbol{\tau_{e-ph}}$ at different pump fluences are plotted as a function of the absorbed energy density (J m^{-3}) (figure 3(b)). The absorbed energy density for different nanoparticles is calculated from the pump fluence considering the differences in nanoparticle size, optical density and substrate coverage. (details are given in the SI)

For all the nanoparticles, longer electron-phonon decay times are observed with increases in the absorbed energy density and the

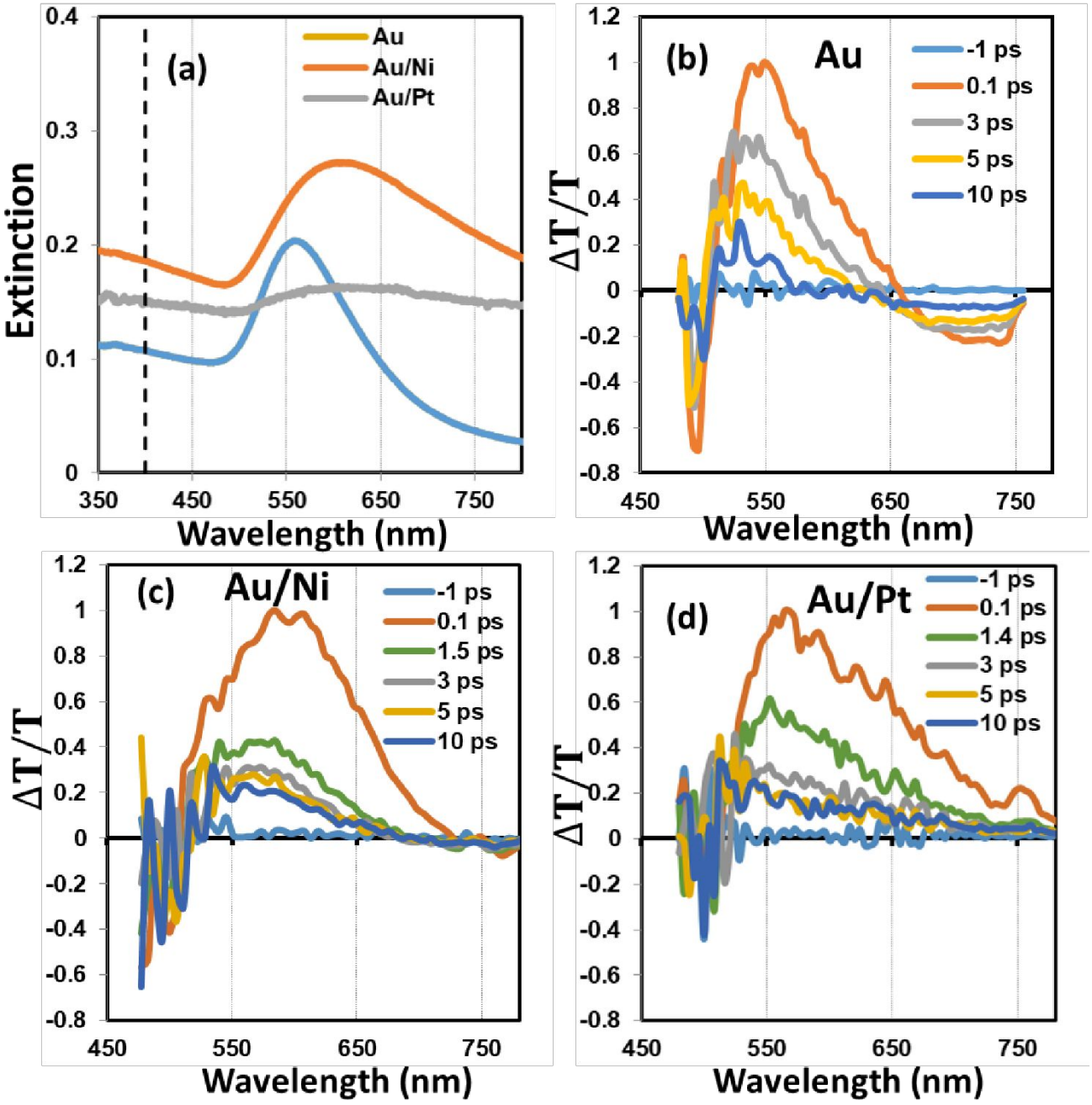

Figure 2: (a) Steady state absorbance of different nanoparticles. The dotted line shows the excitation wavelength of 400 nm used in our transient absorption studies. The normalized differential transmission spectra of (b) Au, (c) Au/Ni and (d) Au/Pt nanoparticles are shown as a function of the time delay between the pump (400 nm) and probe (white light) pulses for a pump fluence of 78 μJ/cm^2.

resulting higher initial electronic temperatures, as expected from equation (1). Interestingly, throughout the measured range both Au/Pt and Au/Ni nanoparticles exhibit faster dynamics than that of bare Au nanoparticles (Figure 3(b)). Our τ_{e-ph} vs. absorbed energy density data can be fit well with a straight line, confirming the validity of using the two-temperature model to explain our experimental data. We can extract the energy density-independent characteristic electron-phonon coupling time, τ^0_{e-ph}, by extrapolating the linear plots to zero absorbed energy density, where $\tau^0_{e-ph} \approx \frac{\gamma T_1}{g}$.[35, 36, 44]

From figure 3(b), the τ^0_{e-ph} values for Au, Au/Pt and Au/Ni are found to be 0.9 ps, 0.4 ps and 0.4 ps, respectively. In this limit, $\tau^0_{e-ph}$is only a function of the electron-phonon coupling constant g and the electronic heat capacity γ. It is an intrinsic property of the material and can be used to understand the effect of the composition of different nanoparticles on electron-phonon coupling. [38, 43]

We note that over the size range of nanoparticles studied here and at the pump fluence used in our experiments, variations in the size or shape of the bimetallic nanoparticles are not expected to significantly influence their electron-phonon coupling time.[39, 45] Size effects on the electron-phonon relaxation rate are pronounced if the nanoparticle size is significantly below the mean free path of the electrons (λ). This is due to the interaction between the electrons

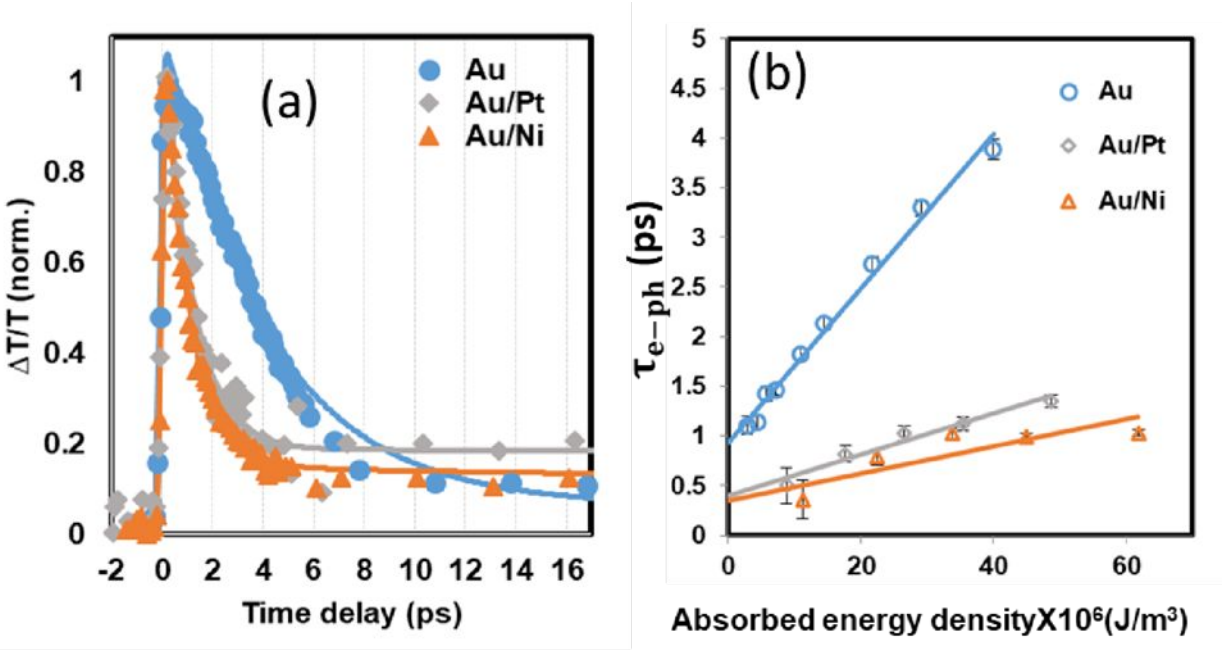

Figure 3: (a) Normalized differential transmission (ΔT/T) traces for different samples. The pump fluence for each sample is fixed to obtain an absorbed pump-photon number density of $7.5 \times 10^{18}\ cm^{-3}$. The probe wavelength is set to the peak of the normalized differential transmission spectra shown in figure 2 for each sample. (b) Electron-phonon decay time constant for different nanoparticles as a function of absorbed energy density.

and the surface phonons in the nanoparticles. However, the contribution of electron-surface phonon coupling is also proportional to the ratio of the metal atomic valence to its atomic mass, (n/m).[46] Even though the mean free path of electrons in gold is 37.7 nm,[47] the influence of nanoparticle size and shape on the electron-phonon scattering rate is not pronounced until the size falls below 10 nm. This is attributed to the relatively small contributions of electron-surface phonon coupling for gold because of the low n/m value (.01). The n/m values for nickel and platinum are .07 and .03 respectively, which are relatively higher than gold. However, their mean free paths for electrons are significantly less than gold, 10 nm for Pt and 5.87 nm for Ni. [47] Additionally, it has been found that even for bimetallic nanoparticles, variations in size and shape do not alter the electron-phonon scattering time until the pump fluence is as high as 2800 μJ/cm^2, which is much higher than the pump fluence used in our experiments.[42]

In order to verify our experimental observations, we used values of $\boldsymbol{\gamma}$ and g for Au, Pt and Ni from the literature to theoretically estimate their $\boldsymbol{\tau^0_{e-ph}}$ values. The effective $\boldsymbol{\tau^0_{e-ph}}$for the bimetallic nanoparticles was calculated using a phenomenological model:[44]

$$\frac{1}{\tau^0_{e-ph}(Au/X)} = \frac{\alpha_{Au}}{\tau^0_{e-ph}(Au)} + \frac{1-\alpha_{Au}}{\tau^0_{e-ph}(x)} \quad (3)$$

According to the above equation, the electron-phonon coupling time of the bimetallic Au/X particles can be calculated as an average of the electron-phonon coupling times of Au and the other metal X, weighted by the density of electronic states of each. $\boldsymbol{\alpha_{Au}}$ is the fraction of electronic states due to Au, which can be calculated using the following equation,

$$\boldsymbol{\alpha_{Au}} = \frac{x_{Au} \times \rho(\epsilon_F)_{Au}}{x_{Au} \times \rho(\epsilon_F)_{Au} + (1-x_{Au}) \times \rho(\epsilon_F)_X} \quad (4)$$

where $\boldsymbol{x_{Au}}$ is the atomic mole fraction of Au in the bimetallic nanoparticles, and $\boldsymbol{\rho(\epsilon_F)_{Au}}$ and $\boldsymbol{\rho(\epsilon_F)_X}$ are the density of electronic states at the Fermi level for Au and the other metal *X*, respectively. In this calculation, we assumed the temperature of the lattice to be 300 K. At that temperature the electron-phonon coupling constants, *g*, for Au, Pt, and Ni are 2.6 × 10^{16} Wm^{-3}K^{-1}, 1 × 10^{18} Wm^{-3}K-1, and 1 × 10^{18} Wm^{-3}K^{-1}, respectively.[48] The electronic heat capacities, $\boldsymbol{\gamma}$ for Au, Pt and Ni are 67 Jm^{-3}K,$^{-2}$, 464 Jm^{-3}K^{-2} and 1230 Jm^{-3}K^{-2}, respectively. The density of states for Au, Pt and Ni at the Fermi energy is 0.3 states/eV/atom, 2.2 states/eV/atom and 5 states/eV/atom, respectively.[48] Using these values, the theoretically calculated $\boldsymbol{\tau^0_{e-ph}}$values for Au, Au/Pt and Au/Ni were found to be 0.77 ps, 0.47 ps and 0.33 ps, respectively. We also calculated the values for pure Pt and Ni nanoparticles for comparison (0.35 ps and 0.13 ps, respectively). While the above values calculated using our simple phenomenological model are not expected to exactly match our experimental observations, they do qualitatively match our experimental findings. Both our theoretical and experimental observations show that $\boldsymbol{\tau^0_{e-ph}}$for Au/Pt and Au/Ni nanoparticles is significantly shorter than that for Au, which is primarily attributed to the significantly larger (~40 times) *g* values of Pt and Ni in comparison to Au. While the γ values of Pt and Ni are higher than Au, the ratio γ/*g* is still significantly higher for Au in comparison to Pt and Ni. Additionally, both Ni and Pt have a larger density of electronic states at the Fermi level than gold. Hence, even with the low content of Pt or Ni in the bimetallic nanoparticles, the decay responses of the Au/Pt and Au/Ni nanoparticles are significantly influenced by Pt and Ni.

We next investigate the ΔT traces on longer time scales. Dots in figure 4(a) show the measured ΔT traces for the three different

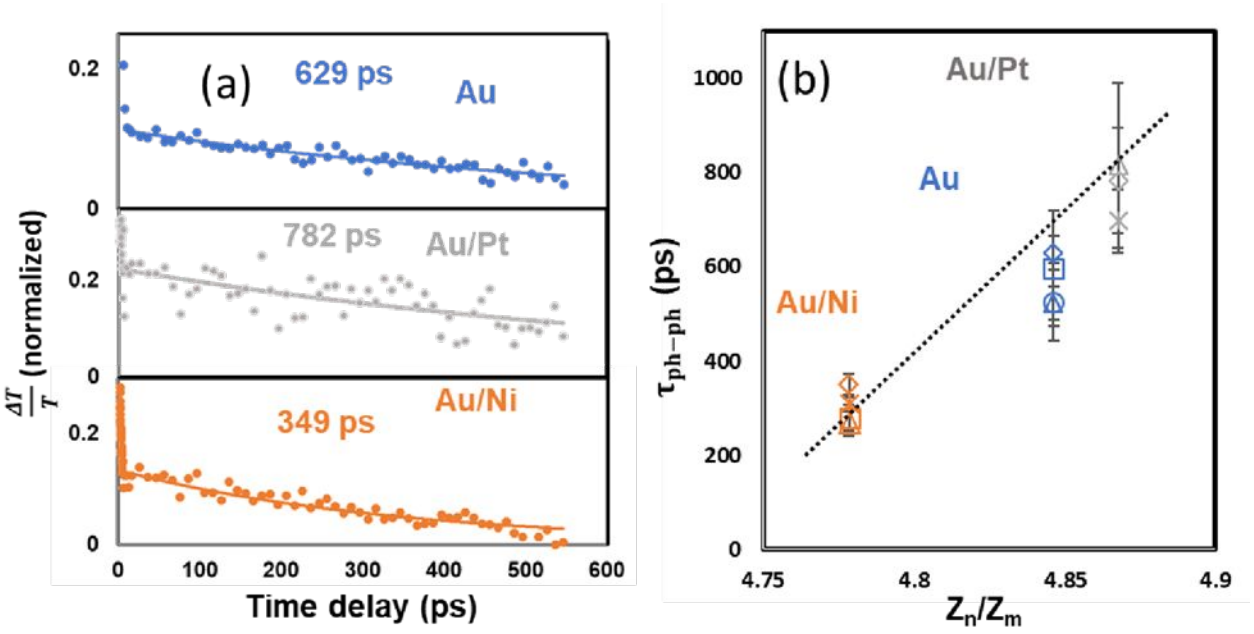

Figure 4: (a) Differential transmission (ΔT/T) dynamics on a long time scale. Dots are normalized ΔT traces and black lines are exponential fits. The probe wavelength is at the peak of the normalized ΔT spectra shown in figure 2 for each sample. The pump fluence for each sample is fixed to obtain an absorbed pump-photon number density of $7.5 \times 10^{18}\ cm^{-3}$. (b) Phonon-phonon coupling time (τ_{ph-ph}) as a function of the acoustic impedance mismatch (Z_n/Z_m). Symbol shapes represent the absorbed pump-photon densities: $2 \times 10^{18}\ cm^{-3}$(□), $3 \times 10^{18} cm^{-3}$(○), $5 \times 10^{18} cm^{-3}$(△), $7.5 \times 10^{18} cm^{-3}$(×), and $10 \times 10^{18} cm^{-3}$(◊). The dashed line is a guide to the eye.

nanoparticles. The pump fluence was adjusted for each sample to fix the absorbed pump-photon number density (~$\boldsymbol{7.5 \times 10^{18}\ cm^{-3}}$), following the absorbance data in Figure 2(a). We can see that the sub-10 ps e-ph thermalization discussed above is followed by a slow decay for all the samples, which is generally attributed to phonon-phonon coupling.[35] We used exponential fits (lines in figure 4(a)) to obtain the phonon-phonon coupling time ($\boldsymbol{\tau_{ph-ph}}$), which ranges from ~350 ps to ~800 ps, in reasonable agreement with previous studies.[35, 36]

The key result here is that $\boldsymbol{\tau_{ph-ph}}$ largely varies depending on the type of nanoparticle. $\boldsymbol{\tau_{ph-ph}}$ represents the timescale for heat release from nanoparticles to the substrate via coupling between their lattice vibrational modes. This cooling process includes heat transfer at the nanoparticle-substrate interface and heat diffusion within the substrate. The latter should be similar for all samples because the same kind of glass substrate (fused silica) is used. Thus, the observed $\boldsymbol{\tau_{ph-ph}}$ can be assumed to reflect the relative heat transfer efficiencies at the different nanoparticle-substrate interfaces. It is known that the interfacial thermal resistance is approximately proportional to the acoustic impedance (*Z*) mismatch between the nanoparticle and matrix, $\boldsymbol{Z_n/Z_m}$, where the subscript *n* (*m*) represents the nanoparticle (matrix).[41, 49] In figure 4b, we plot $\boldsymbol{\tau_{ph-ph}}$ as a function of $\boldsymbol{Z_n/Z_m}$ by using *Z* values found in literature; $\boldsymbol{Z_n}$ can be estimated using a weighted average, *Z,* for Au ($\boldsymbol{63 \times 10^6}$ kg m^{-2}s^{-1}) and for Pt ($\boldsymbol{70 \times 10^6}$ kg m^{-2}s^{-1}) or Ni ($\boldsymbol{41 \times 10^6}$ kg m^{-2}s^{-1}), and $\boldsymbol{Z_m}$ for the glass substrate is known to be $\boldsymbol{13 \times 10^6}$ kg m^{-2}s^{-1}.[42,50,51] We can see that $\boldsymbol{\tau_{ph-ph}}$ is roughly proportional to $\boldsymbol{Z_n/Z_m}$, regardless of absorbed photon density. This suggests that there is a relationship between the long decay component and the heat transfer efficiency at the nanoparticle-substrate interface. We note that the observed dependence of $\boldsymbol{\tau_{ph-ph}}$ on the nanoparticle type in Figure 4(b) is unlikely to be due to variations in the NP size, although the nanoparticle diameter slightly varies with the material type (Figures. 1(d)-1(f)). Generally, $\boldsymbol{\tau_{ph-ph}}$ increases with the nanoparticle size, because the time for heat to reach the nanoparticle-substrate interface is approximately proportional to the nanoparticle diameter.[52] However, the observed $\boldsymbol{\tau_{ph-ph}}$ values for bare Au NPs with the smallest average diameter are larger than those for Au/Ni, as shown in Figure 4(b), suggesting that the nanoparticle size is not a critical factor in causing the material dependence of $\boldsymbol{\tau_{ph-ph}}$, and instead $\boldsymbol{\tau_{ph-ph}}$ is dominated by the acoustic impedance mismatch at the interface. It should be noted that we didn't see any effect of absorbed photon density on $\boldsymbol{\tau_{ph-ph}}$. This may be due to the fact that at the pump fluence used for the measurements, the maximum temperature rise of the thermalized electrons is negligible (see section 1 in the SI for the calculation).

Conclusions:

In summary, we have demonstrated that the relaxation dynamics of multicomponent bimetallic plasmonic nanoparticles are a strong function of their composition. Our ultrafast transient absorption spectroscopy studies revealed that the addition of catalytic components, such as platinum or nickel, to plasmonic gold can significantly enhance the electron-phonon coupling rate. Similarly, the phonon-phonon coupling rate of bimetallic Au/Pt and Au/Ni nanoparticles was significantly different than that of pure gold nanoparticles, due to the acoustic impedance mismatch at the nanoparticle/substrate interface. Our findings have important implications for the design of multicomponent plasmonic nanocatalysts. Electron-phonon and phonon-phonon coupling in

nanoparticles significantly influences their efficiency in local photothermal heat generation and also hot electron transfer.[3] Our work suggests that tailoring the composition of a plasmonic catalyst will not only tune their light absorption, but also enable us to control their relaxation dynamics to maximize their catalytic efficiency when driven by light, with important implications for their use in industry-relevant reactions.

Conflicts of interest

There are no conflicts to declare.

Supporting Information Description:

Supporting information is available. Different properties of Au, Pt and Ni. Histogram to show size distribution for Au, Au/Pt and Au/Ni nanoparticles. Theoretically calculated absorbance of Au, Au/Ni and Au/Pt nanoparticles. Methods to calculate maximum temperature rise of the thermalized electrons and absorbed energy density.

Acknowledgements:

This work was performed, in part, at the Center for Integrated Nanotechnologies, an Office of Science User Facility operated for the U.S. Department of Energy (DOE) Office of Science by Los Alamos National Laboratory (Contract DE-AC52-06NA25396) and Sandia National Laboratories (Contract DE-NA-0003525). The authors want to thank the DOE VFP program for summer scholarship and Ying-Bing Jiang for TEM assistance.

Notes and references

1. S. Mukherjee, F. Libisch, N. Large, O. Neumann, L. V. Brown, J. Cheng, J. B. Lassiter, E. A. Carter, P. Nordlander and N. J. Halas, *Nano letters*, 2013, **13**, 240-247.
2. S. Linic, P. Christopher and D. B. Ingram, *Nature materials*, 2011, **10**, 911-921.
3. H. Huang, L. Zhang, Z. Lv, R. Long, C. Zhang, Y. Lin, K. Wei, C. Wang, L. Chen, Z. Y. Li, Q. Zhang, Y. Luo and Y. Xiong, *J Am Chem Soc*, 2016, **138**, 6822-6828.
4. R. Long, Z. Rao, K. Mao, Y. Li, C. Zhang, Q. Liu, C. Wang, Z. Y. Li, X. Wu and Y. Xiong, *Angew Chem Int Ed Engl*, 2015, **54**, 2425-2430.
5. F. Wang, C. Li, H. Chen, R. Jiang, L. D. Sun, Q. Li, J. Wang, J. C. Yu and C. H. Yan, *J Am Chem Soc*, 2013, **135**, 5588-5601.
6. J. R. Adleman, D. A. Boyd, D. G. Goodwin and D. Psaltis, *Nano Lett.*, 2009, **9**, 4417-4423.
7. L. Guo, Q. Sun, K. Marcus, Y. Hao, J. Deng, K. Bi and Y. Yang, *J. Mater. Chem. A*, 2018, **6**, 22005-22012.
8. J. M. Walker, L. Gou, S. Bhattacharyya, S. E. Lindahl and J. M. Zaleski, *Chem. of Mater.*, 2011, **23**, 5275-5281.
9. K. M. Haas and B. J. Lear, *Chem Sci*, 2015, **6**, 6462-6467.
10. D. Han, Z. Bao, H. Xing, Y. Yang, Q. Ren and Z. Zhang, *Nanoscale*, 2017, **9**, 6026-6032.
11. J. N. G. Stanley, I. García-García, T. Perfrement, E. C. Lovell, T. W. Schmidt, J. Scott and R. Amal, *Chem. Eng. Sci.*, 2019, **194**, 94-104.
12. U. Aslam, S. Chavez and S. Linic, *Nature Nanotechnology*, 2017, **12**, 1000-1005.
13. Y. Chen, Y. Zhai, L. Deng, N. Wang, Y. Mao, J. Yang and Y. Huang, *Appl. Phys. Lett.*, 2019, **114**, 183902.
14. W. He, X. Wu, J. Liu, K. Zhang, W. Chu, L. Feng, X. Hu, W. Zhou and S. Xie, *Langmuir*, 2010, **26**, 4443-4448.
15. S. Guo, J. Li, S. Dong and E. Wang, *J. Phys. Chem. C*, 2010, **114**, 15337-15342.
16. J. N. G. Stanley, I. García-García, T. Perfrement, E. C. Lovell, T. W. Schmidt, J. Scott and R. Amal, *Chemical Engineering Science*, 2019, **194**, 94-104.
17. P. Han, T. Tana, Q. Xiao, S. Sarina, E. R. Waclawik, D. E. Gómez and H. Zhu, *Chem*, 2019, **5**, 2879-2899.
18. Z. Zheng, T. Tachikawa and T. Majima, *Journal of the American Chemical Society*, 2014, **136**, 6870-6873.
19. H. Song, X. Meng, T. D. Dao, W. Zhou, H. Liu, L. Shi, H. Zhang, T. Nagao, T. Kako and J. Ye, *ACS Applied Materials & Interfaces*, 2018, **10**, 408-416.
20. W. Hou and S. B. Cronin, *Adv. Funct. Mater.*, 2013, **23**, 1612-1619.
21. C. Gong and M. S. Leite, *ACS Photon.*, 2016, **3**, 507-513.
22. S. Chowdhury, V. R. Bhethanabotla and R. Sen, *Appl. Phys. Lett.*, 2009, **95**, 131115.
23. P. G. Alyssa Beierle , Hanqing Pan, Michael D. Heagy, Alejandro Manjavacas, Sanchari Chowdhury, *Sol Energy Mater Sol Cells*, 2019, **200**, 109967.
24. A. Manjavacas, J. G. Liu, V. Kulkarni and P. Nordlander, *ACS Nano*, 2014, **8**, 7630-7638.
25. L. Zhou, C. Zhang, M. J. McClain, A. Manjavacas, C. M. Krauter, S. Tian, F. Berg, H. O. Everitt, E. A. Carter, P. Nordlander and N. J. Halas, *Nano Lett.*, 2016, **16**, 1478-1484.
26. A. E. Schlather, A. Manjavacas, A. Lauchner, V. S. Marangoni, C. J. DeSantis, P. Nordlander and N. J. Halas, *J Phys. Chem. Lett.*, 2017, **8**, 2060-2067.
27. D. G. Cahill, P. V. Braun, G. Chen, D. R. Clarke, S. Fan, K. E. Goodson, P. Keblinski, W. P. King, G. D. Mahan, A. Majumdar, H. J. Maris, S. R. Phillpot, E. Pop and L. Shi, *App. Phys. Rev.*, 2014, **1**, 011305.
28. M. Shabaninezhad, A. Abuhagr, N. A. Sakthivel, C. Kumara, A. Dass, K. Kwak, K. Pyo, D. Lee and G. Ramakrishna, *J. Phys. Chem. C*, 2019, DOI: 10.1021/acs.jpcc.9b01739.
29. Sudheer, P. Mondal, V. N. Rai and A. K. Srivastava, *AIP Adv.*, 2017, **7**, 075303.
30. A. Wilson, R. Bernard, A. Vlad, Y. Borensztein, A. Coati, B. Croset, Y. Garreau and G. Prévot, *Phys. Rev.B*, 2014, **90**, 075416.
31. D. Chen, J. Li, C. Shi, X. Du, N. Zhao, J. Sheng and S. Liu, *Chem. Mater.*, 2007, **19**, 3399-3405.
32. L. Qian, Y. Sha and X. Yang, *Thin Sol. Films*, 2006, **515**, 1349-1353.
33. S. Mandal, A. B. Mandale and M. Sastry, *J. Mater. Chem. A*, 2004, **14**, 2868-2871.

34. J. A. Creighton and D. G. Eadon, *J. Chem. Soc. Faraday Trans*, 1991, **87**, 3881-3891.
35. G. V. Hartland, *Chemical Rev.*, 2011, **111**, 3858-3887.
36. S. L. and and M. A. El-Sayed, *Annu Rev. Phys. Chem.*, 2003, **54**, 331-366.
37. D. J. Hilton and C. L. Tang, *Phys. Rev. Lett.*, 2002, **89**, 146601.
38. J. H. Hodak, A. Henglein and G. V. Hartland, *J Phys. Chem. B*, 2000, **104**, 9954-9965.
39. S. Link, C. Burda, M. B. Mohamed, B. Nikoobakht and M. A. El-Sayed, *Phys. Rev. B*, 2000, **61**, 6086-6090.
40. M. Broyer, E. Cottancin, J. Lermé, M. Pellarin, N. Del Fatti, F. Vallée, J. Burgin, C. Guillon and P. Langot, *Faraday Discuss.*, 2008, **138**, 137-145.
41. V. Juvé, M. Scardamaglia, P. Maioli, A. Crut, S. Merabia, L. Joly, N. Del Fatti and F. Vallée, *Phys. Rev.B*, 2009, **80**, 195406.
42. H. F. Zarick, A. Boulesbaa, E. M. Talbert, A. Puretzky, D. Geohegan and R. Bardhan, *J. Phys. Chem. C*, 2017, **121**, 4540-4547.
43. G. V. Hartland, *Chem Rev*, 2011, **111**, 3858-3887.
44. J. H. Hodak, A. Henglein and G. V. Hartland, *J. Chem. Phys.*, 2001, **114**, 2760-2765.
45. W. Huang, W. Qian, M. A. El-Sayed, Y. Ding and Z. L. Wang, *J. Phys. Chem. C*, 2007, **111**, 10751-10757.
46. W. Huang, W. Qian, M. A. El-Sayed, Y. Ding and Z. L. Wang, *The Journal of Physical Chemistry C*, 2007, **111**, 10751-10757.
47. D. Gall, *Journal of Applied Physics*, 2016, **119**, 085101.
48. S. Ishii, R. P. Sugavaneshwar and T. Nagao, *J. Phys. Chem. C*, 2016, **120**, 2343-2348.
49. D. G. Cahill, W. K. Ford, K. E. Goodson, G. D. Mahan, A. Majumdar, H. J. Maris, R. Merlin and S. R. Phillpot, *J. Appl. Phys.*, 2003, **93**, 793-818.
50. C. Voisin, D. Christofilos, N. Del Fatti and F. Vallée, *Physica B: Cond. Matt.*, 2002, **316-317**, 89-94.
51. A. Gill, A. Telang, S. R. Mannava, D. Qian, Y.-S. Pyoun, H. Soyama and V. K. Vasudevan, *Mater. Sci. Eng. A*, 2013, **576**, 346-355.
52. O. M. Wilson, X. Hu, D. G. Cahill and P. V. Braun, *Physical Review B*, 2002, **66**, 224301.

The charge carrier relaxation dynamics of bimetallic plasmonic catalysts Au/Ni and Au/Pt are significantly different than that of pure Au nanoparticles, which will impact their performance.

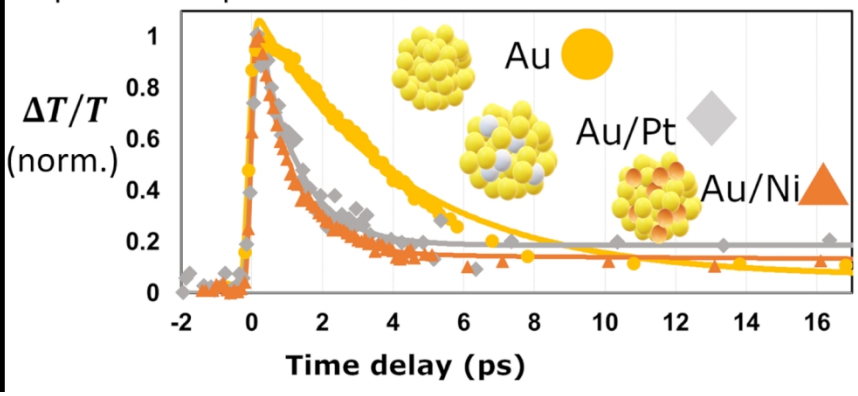

69x38mm (600 x 600 DPI)